Supporting information

Quantum Dynamics Simulations Reveal Ultrafast and Coherent Charge Transfer in the Lhca4 antenna of Photosystem I

Piermarco Saraceno,[†] Fabrizio Santoro,[*,‡] and Lorenzo Cupellini[*,†]

[†]Department of Chemistry and Industrial Chemistry, University of Pisa, 56124 Pisa, Italy

[‡]Institute of Chemistry of Organometallic Compounds (ICCOM-CNR), CNR Research Area, 56124 Pisa, Italy

E-mail: fabrizio.santoro@pi.iccom.cnr.it; lorenzo.cupellini@unipi.it

S1 Quantum dynamics

To simulate the wavepacket dynamics, the vibronic wavefunction is expressed combining the products of stationary electronic functions $|i\rangle$ and evolving nuclear functions $\left|\Psi_i^{vib}\right\rangle$:

$$|\Psi(\mathbf{q},t)\rangle = \sum_i c_i(t)\,|i\rangle \left|\Psi_i^{vib}\right\rangle(\mathbf{q},t) \tag{S1}$$

The vibrational part is written using the ML-MCTDH ansatz. The nuclear physical coordinates $\mathbf{q} = \{q_1, \ldots, q_f\}$, are compressed in a set of logical coordinates $\mathbf{Q} = \{\mathbf{Q}_1, \ldots \mathbf{Q}_p\}$, each one being a combination of physical coordinates $\mathbf{Q}_k = \{q_{1_k}, \ldots, q_{d_k}\}$. The resulting wavefunctions are:[1–4]

$$\left|\Psi_i^{vib}\right\rangle(\mathbf{Q},t) = \sum_{j_1}^{n_1} \cdots \sum_{j_p}^{n_p} A^{i,1,1}_{j_1 \cdots j_p}(t) \left|\varphi^{i,1,1}_{j_1}(Q_1,t)\right\rangle \ldots \left|\varphi^{i,1,p}_{j_p}(Q_p,t)\right\rangle \tag{S2}$$

where the time-dependent coefficient $A^{i,1,1}_{j_1 \cdots j_p}(t)$ is used to weight the Hartree product

$$\left|\varphi^{i,1,1}_{j_1}(Q_1,t)\right\rangle \ldots \left|\varphi^{i,1,p}_{j_p}(Q_p,t)\right\rangle$$

Each function φ is a multi-dimensional single particle function (SPF), written as a nested expansion of SPFs of lower-dimensionality, where at the lowest level there is the time-independent primitive basis set $\chi(q_i)$ of the individual modes. For a simple three-layer ML-MCTDH wavefunction, the next (and last) layer would be:

$$\left|\varphi^{i,1,k}_{m}(Q_k,t)\right\rangle = \sum_{j_{1_k}}^{N_{1_k}} \cdots \sum_{j_{d_k}}^{N_{d_k}} A^{i,2,k}_{j_{1_k} \cdots j_{d_k}}(t) \left|\chi^{i,k,1}_{j_{1_k}}(q_{1_k})\right\rangle \ldots \left|\chi^{i,k,d_k}_{j_{d_k}}(q_{d_k})\right\rangle \tag{S3}$$

In this work, we use up to 5 layers, where each φ is written in term of lower-layer functions φ, and the functions χ are included in the lowest-layer SPFs.

S2 Adiabaticity of the CT process

To further investigate the adiabatic nature of the dynamics, we calculate the density matrix in the adiabatic basis. Although we cannot access an adiabatic basis along the wavepacket dynamics, we approximate this basis by diagonalizing at each time step the Hamiltonian computed at the expectation values of the normal mode coordinates. The resulting time-dependent eigenstates are used to approximate the adiabatic basis at time t, and the corresponding transformation coefficients $\tilde{c}(t)$ are then used to express the density matrix in this basis:

$$\rho_{ab}^{el,adiab}(t) = \sum_{ij} \tilde{c}_{ia}(t)\tilde{c}_{jb}(t)\rho_{ij}^{el}(t) \tag{S4}$$

For this analysis, we consider the two edge cases for the LE-CT energy gap (i.e. two snapshots) named "case 1" and "case 2", whose potential energy surfaces are shown in Fig. 3b,d. The results are shown in Fig. S1. In both cases, our initial excitation mainly populates the S_1 state, while the other adiabatic states remain essentially unpopulated throughout the dynamics. This observation further confirms that the CT process is essentially adiabatic.

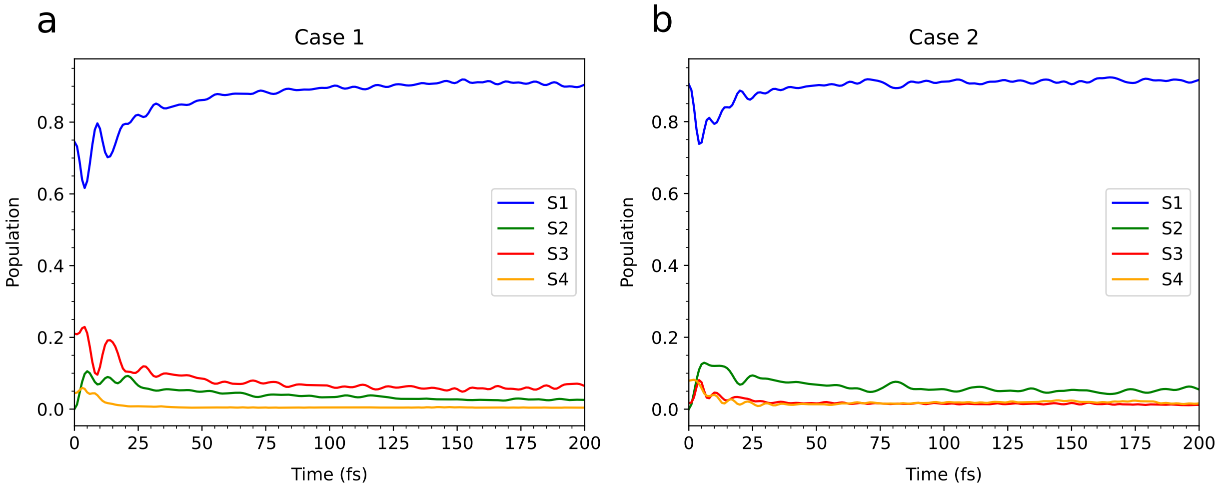

Figure S1: *Adiabatic populations dynamics calculated using the ML-MCTDH method for the a603-a609 dimer, with the initial state set on the lowest bright delocalized state* ex_1. *To convert the population to the adiabatic basis, we follow Eq. S4. The results are averaged over the Molecular Dynamics simulation (MD2 of Ref. 5).*

To explore how the choice of the initial state affects the adiabaticity of the process, we repeat the simulations starting from ex_2, which in both cases has a mainly LE nature. Now, the ultrafast dynamics shows a transfer from ex_2 to ex_1 (see Fig. S2a,b), associated with a more pronounced purity loss during the transfer ($\mathrm{Tr}(\rho^2)$ $\sim$ 0.5, Fig. S2c,d) than what was observed when starting from the bright exciton ($\mathrm{Tr}(\rho^2)$ $\sim$ 0.6, Fig. 2c). The purity recovery is also slower, especially in case 2. These observations suggest that, when the initial population is set on ex_2, the process is nonadiabatic. It is reasonable to think that ex_2 is not populated by interaction with light, as ex_1 borrows most of the dipole (see Fig. S15). On the other hand, if ex_2 were populated by EET from other Chls, it would decay to ex_1 within 50-100 fs and finally reach the same state.

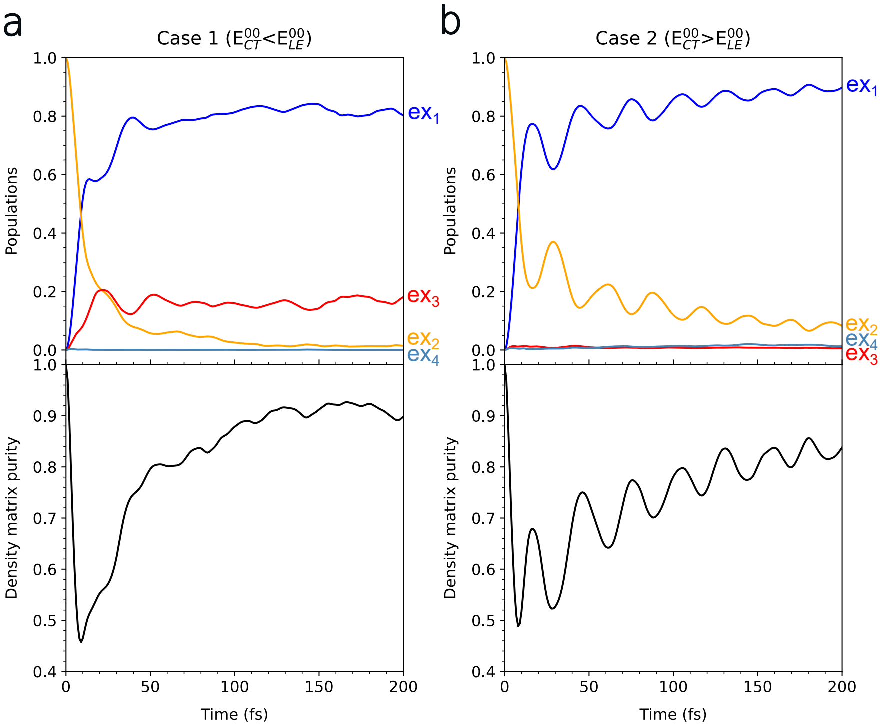

Figure S2: *Populations dynamics (upper plots) and (c,d) density matrix purity (lower plots) for two MD frames (MD2 of Ref. 5), one (a) where the 0-0 energy of the CT state is lower than the LE states, and another (b) showing the opposite case. The initial state is set on* ex_2.

S3 Basin-Hopping Simulations

To find all the possible local minima of the S_1 state, we perform basin-hopping simulations,[6] a global optimization technique to explore energy landscapes. The method alternates between random structural perturbations (”hops”) and local geometry optimizations, allowing the system to escape local minima and sample a wide portion of the PES. To perform these simulations, we use the `basinhopping` function from the `scipy.optimize` Python library.[7] Each simulation consisted of 100 basin-hopping cycles. The value of the T parameter in the `scipy.optimize.basinhopping` function was set to 10000 in order to enhance sampling of the configurational space and reduce the risk of trapping in local minima. Remarkably, all simulations consistently converged to the same minimum structure on the S_1 surface, regardless of the random perturbations applied during the hopping steps.

To further validate this result, we repeat the entire basin-hopping protocol, starting from four different initial geometries, corresponding to the minima of the four diabatic states. We repeat the simulations for all protein conformations extracted from MD2. For each protein conformation, the same S_1 minimum was consistently found across all basin-hopping cycles. These results support the conclusion that the S_1 PES exhibits a single minimum for each fixed protein conformation, with no indication of additional local minima within the explored configurational space.

S4 Comparison with dissipative quantum dynamics

To verify our main conclusions, the ultrafast timescale and coherence of the charge transfer observed in ML-MCTDH simulations, we perform complementary open quantum systems dynamics simulations using the hierarchical equations of motion (HEOM) method.[8] Unlike ML-MCTDH, HEOM naturally incorporates environmental dissipation. If HEOM reproduces similar dynamics — particularly the CT timescale and coherence recovery — this would support the physical validity of the mechanism proposed.

The simulations are carried out for the two representative configurations introduced in Fig. 3, referred to as Case 1 and Case 2, where the a603$^+$a603$^-$ minimum is lower and higher respectively in energy than the LE states.

S4.1 HEOM models

To make HEOM simulations feasible, we had to introduce several simplifications to the LVC model. To reduce computational cost, we exclude the high-energy CT state $a603^{-}a609^{+}$, which was shown to be negligibly populated in ML-MCTDH simulations. The system thus includes the two locally excited states $a603^{*}$ and $a609^{*}$, and the low-energy CT state $a603^{+}a609^{-}$. The bath is constructed starting from the full 427-mode LVC model. The bath modulates the electronic energies, while we neglect the modulation of electronic couplings. Each normal mode is then mapped to a shifted Drude-Lorentz (sDL) spectral density (SD):[9,10]

$$J(\omega) = \pi\lambda_0\omega\gamma \left[\frac{1}{(\omega-\omega_0)^2+\gamma^2} + \frac{1}{(\omega+\omega_0)^2+\gamma^2}\right] \tag{S5}$$

where λ_0 and ω_0 are the reorganization energy and frequency of each mode, respectively, and $\gamma = 350\,\mathrm{cm}^{-1}$ is the damping constant. The parameters are taken from Fig. S8, which leads to a total spectral density for each electronic state, reported in Fig. S3 with an orange line. With blue lines, we also report the SDs obtained using γ=40 cm^{-1}.

We fit the resulting spectral densities using two reduced models. The first, referred to as **HEOM-3**, uses three effective sDL oscillators per diabatic state (parameters in Table S1). The second, referred to as **HEOM-4/5**, is larger and uses four oscillators for each LE state and five for the CT state (parameters in Table S2). The resulting spectral densities are reported in Fig. S3 as solid green and red dashed lines respectively. These spectral densities exactly reproduce the total reorganization energy for each state, and further mimic the distribution of reorganization energies by frequency. However, they introduce additional dissipation in the model, due to the strong damping constants $\gamma > 150$ cm^{-1}. Attempts to run HEOM simulations with lower γ values resulted in population divergence. We couple each electronic state to a different copy of each normal mode. This assumption was shown to be valid in ML-MCTDH simulations (see Fig. S16).

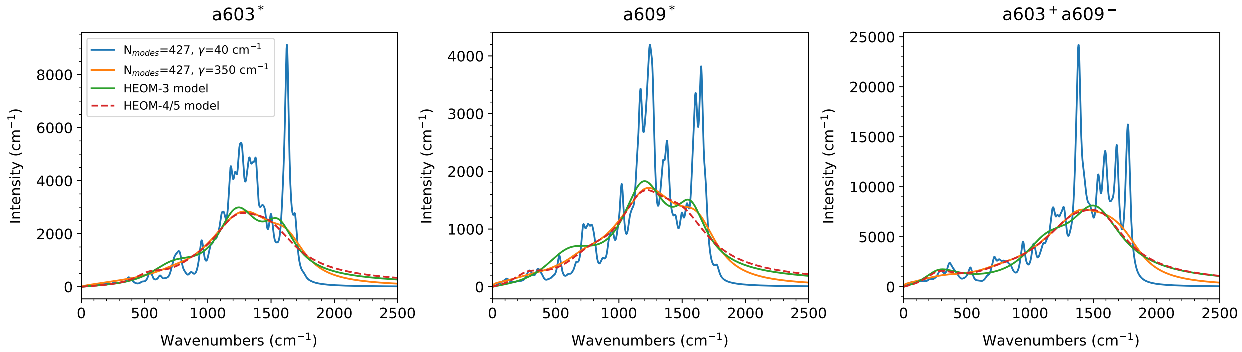

Figure S3: *Spectral densities coming from the models used for the HEOM simulations and ML-MCTDH simulations. Each panel represent the spectral densities of different diabatic electronic states (a603*,a609*,a603$^+$a609$^-$). Blue and orange lines indicate the spectral densities obtained starting from the full 427 modes model (parameters in Fig. S8), and mapping each mode to a sDL oscillator (Eq. S5), with γ=40,350 cm^{-1} for the blue and orange lines respectively. Solid green (dashed red) lines indicate the* ***HEOM-3*** *(****HEOM-4/5****) sDL model, whose parameters are reported in Table S1 (Table S2).*

S4.2 HEOM convergence

To perform HEOM simulations, we use a distributed-memory implementation (DM-HEOM), which enables scalable and high-performance computations.[11] With the **HEOM-4/5** model, populations diverge after ∼15-20 fs for hierarchy depths up to 7 (Fig. S4a). The calculation at depth 8 became stable; however, a further increase of the hierarchy depth was impossible because of memory requirements exceeding 250 GB of RAM, thus preventing us from assessing the convergence. We therefore adopt the **HEOM-3** model, which reaches a reasonable convergence at depth 11, as shown in Fig. S4b,c. Given these results, we proceeded with the **HEOM-3** model.

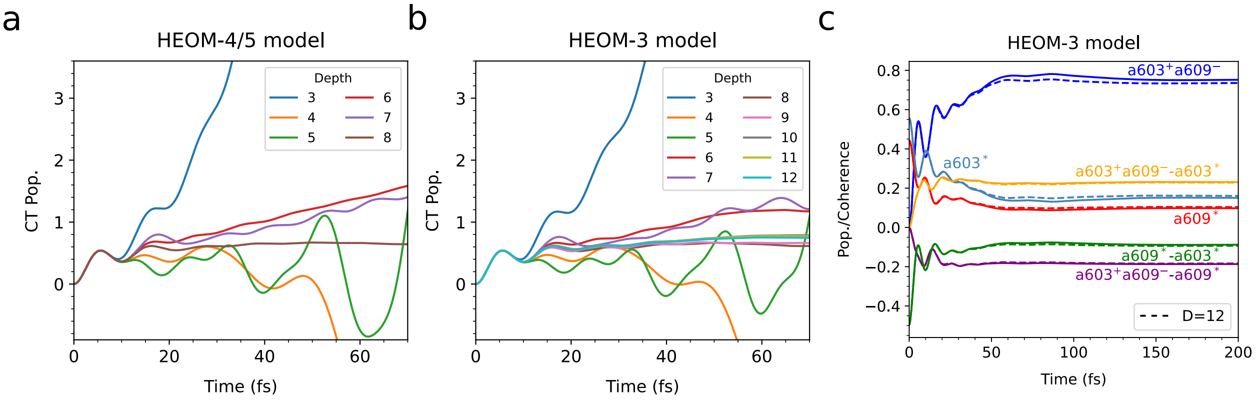

Figure S4: *Convergence calculations on HEOM dynamics. (a,b) HEOM population dynamics of the a603*$^{+}$*a609*$^{-}$ *state obtained with different values for the depth parameters, with the (a)* ***HEOM-4/5*** *and (b)* ***HEOM-3*** *model (parameters in Table S2). (c) Dynamics of all populations and coherences using the* ***HEOM-3*** *model, and depth of 11 (solid lines) and 12 (dashed lines). The simulations are performed at 300 K for the Case 2 of Fig. 3.*

S4.3 Comparison of ML-MCTDH and HEOM

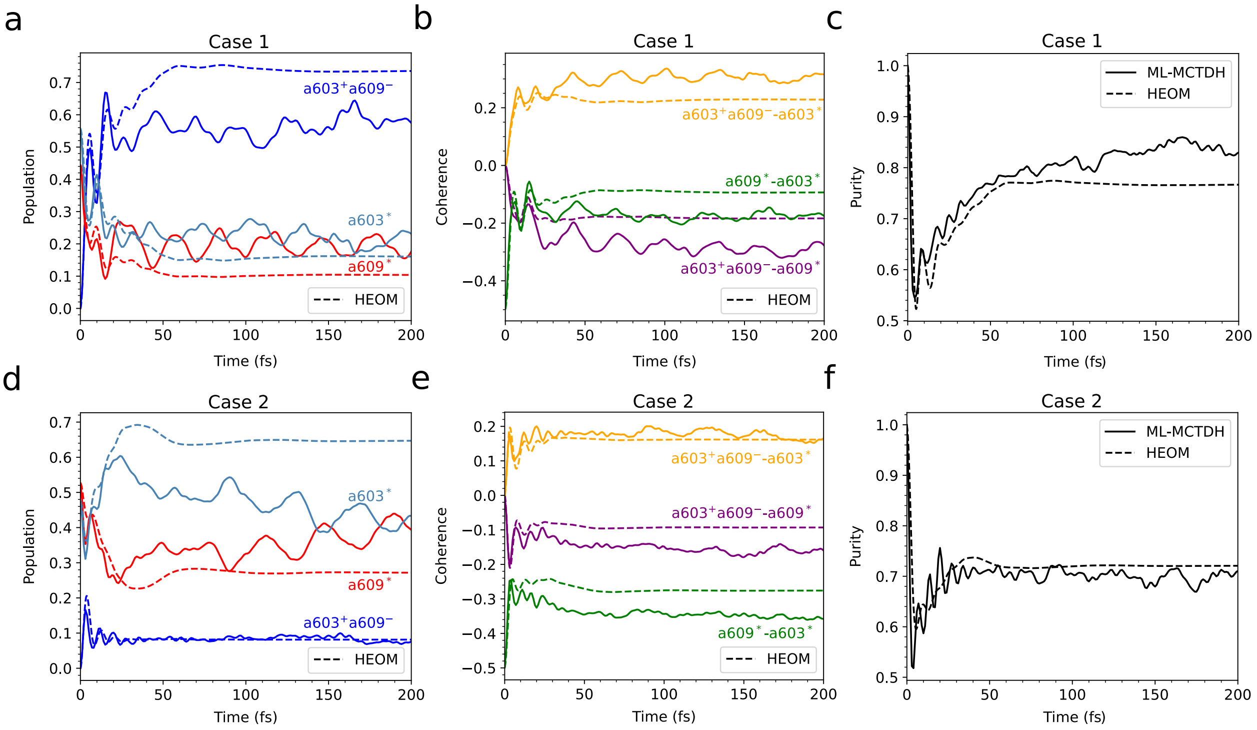

Figure S5: *Comparison between ML-MCTDH (solid lines) and HEOM (dashed lines) dynamics. (a,b,c) Dynamics of the configuration called Case 1 in Fig. 3. (d,e,f) Case 2. (a,d) Population, (b,e) coherence and (c,f) purity dynamics. HEOM simulations are performed setting the depth to 11 and using the* ***HEOM-3*** *model (parameters in Table S1). HEOM simulations are performed at 300 K.*

The resulting HEOM dynamics are compared with ML-MCTDH simulations in Fig. S5, for both Case 1 (top row, panels a,b,c) and Case 2 (bottom row, panels d,e,f). Population dynamics (Fig. S5a,d) show quantitative agreement up to 20-30 fs. After ∼50 fs, ML-MCTDH exhibits persistent oscillations, while HEOM reaches equilibrium due to the dissipation. Both methods preserve coherences at long times (Fig. S5b,e).

Importantly, the purity of the electronic density matrix (Fig. S5c,f) predicted by the two methods is extremely similar. An initial drop in purity is observed due to the separation of vibrational wavepackets across different electronic states, followed by a recovery as the system relaxes toward the unique minimum of the S_1 surface. In Case 1, the purity obtained with HEOM reaches a plateau earlier at about 0.76, while the ML-MCTDH purity reaches ∼0.83 at 200 fs. In contrast, in Case 2, the HEOM purity (∼0.72) is slightly higher than ML-MCTDH results. We can conclude that in both cases, the restoration of purity is not an artifact of the closed-system ML-MCTDH treatment, but rather a feature of the adiabatic relaxation mechanism.

Notably, these results are obtained in spite of the substantially stronger dissipation introduced by our **HEOM-3** model. We can assume that these HEOM simulations provide an upper bound to the dissipation strength in this system. The results of this section confirm that the ultrafast (∼50 fs) and adiabatic nature of the CT process is robust against the inclusion of (strong) environmental dissipation, supporting the mechanistic interpretation proposed in the main text.

Table S1: Shifted Drude-Lorentz parameters (λ, γ, ω_0) of the HEOM-3 model. All parameters are given in cm^{-1}. The parameters were optimized to best reproduce the spectral density obtained from the model shown in Fig. S8.

$a603^*$				$a609^*$				$a603^+a609^-$			
Eff. mode	λ	γ	ω_0	**Eff. mode**	λ	γ	ω_0	**Eff. mode**	λ	γ	ω_0
1	248	250	704	1	239	267	571	1	860	166	250
2	417	205	1220	2	276	215	1180	2	772	250	1116
3	152	154	1555	3	84	148	1560	3	1077	250	1496

Table S2: Shifted Drude-Lorentz parameters (λ, γ, ω_0) of the HEOM-4/5 model (used in Fig. S4a). All parameters are given in cm^{-1}. The parameters were optimized to best reproduce the spectral density obtained from the model shown in Fig. S8.

$a603^*$				$a609^*$				$a603^+a609^-$			
Eff. mode	λ	γ	ω_0	**Eff. mode**	λ	γ	ω_0	**Eff. mode**	λ	γ	ω_0
1	92	150	521	1	99	150	250	1	689	150	250
2	114	250	892	2	122	250	747	2	308	250	764
3	390	250	1205	3	261	250	1171	3	277	250	1067
4	222	250	1476	4	116	250	1492	4	724	250	1311
								5	709	250	1554

S5 Absorption spectra calculations

To validate the Hamiltonians employed in the quantum dynamics simulations, we compute the linear absorption spectrum of Lhca4 and compare it with the experimental one measured at 77 K in Ref. 12. In order to reproduce the absorption spectrum in the Q_y region and to directly compare with experiment, it is essential to include all pigments in the excitonic model. The excitonic parameters for these pigments are taken from Ref. 5 and are obtained from four independent molecular dynamics trajectories (MD1, MD2, MD3, and MD4), for a total of 200 configurations.

We treated the excitonic and CT parts of the Hamiltonian as independent ensembles and generated all possible combinations between them. Each combined Hamiltonian is obtained by augmenting the excitonic Hamiltonian with two additional rows and columns corresponding to the two CT states. The diagonal elements of this block contain the CT state energies, while the off-diagonal elements contain the couplings between the CT states and Chls a603 and a609. The site energies of a603 and a609 and their mutual coupling are replaced by those obtained from the CT calculations. Because two different density-functional approximations were employed for the excitonic (M06-2X) and CT (ωB97XD) calculations, we shift the dimer LE and CT energies so that the average energy of Chls a603 and a609 in the excitonic Hamiltonian matches the corresponding average energy in the final augmented Hamiltonian. Moreover, to compensate for the systematic error of the TD-DFT method, we shift the site energies by -910 cm^{-1} (Chl a and CT states) and -670 cm^{-1} (Chl b). The average Hamiltonian obtained is reported in Table S3. The a603 and a609 transition dipoles are taken from the exciton M06-2X calculations.

Table S3: Exciton Hamiltonian of Lhca4 (averaged over MD1, MD2, MD3, MD4). All data in cm^{-1}. CT1 corresponds to a603^{+}a609^{-}, while CT2 corresponds to a603^{-}a609^{+}. To correct for the different DFT functionals used for the LE and CT calculations, the a603, a609 and CT energies coming from the dimer calculations are shifted to match the a603 and a609 energies from the exciton calculations. The energies are further shifted by -910 cm^{-1} (Chl a and CT states) and -670 cm^{-1} (Chl b).

	a601	a602	a603	a604	b606	b607	b608	a609
a601	15640.2	-26.6	12.4	0.0	0.0	0.0	0.0	-0.0
a602	-26.6	15368.7	44.1	9.1	7.6	8.1	-8.1	-44.8
a603	12.4	44.1	15575.7	-5.7	-10.6	9.8	3.4	273.6
a604	0.0	9.1	-5.7	15535.4	103.6	34.0	-2.3	-7.5
b606	0.0	7.6	-10.6	103.6	16082.0	34.6	-2.8	-3.6
b607	0.0	8.1	9.8	34.0	34.6	16176.1	-5.3	-18.1
b608	0.0	-8.1	3.4	-2.3	-2.8	-5.3	16216.8	49.9
a609	-0.0	-44.8	273.6	-7.5	-3.6	-18.1	49.9	15479.8
a610	-0.1	-15.8	19.4	-3.7	-2.1	1.8	75.6	-8.4
a611	-42.4	-10.7	-1.2	-4.5	0.0	0.0	7.4	6.5
a612	6.9	23.7	-2.8	3.2	2.5	3.3	-0.7	-1.5
a613	2.7	-2.7	4.1	2.0	2.1	3.9	0.0	-5.6
a614	-9.0	0.9	-8.5	-6.2	0.0	-2.9	0.0	0.0
a615	0.0	-2.6	8.3	1.4	-2.0	-4.8	3.8	-10.8
b616	0.0	0.0	-4.0	2.7	-1.3	-0.2	19.4	12.5
CT1	0.0	0.0	-806.6	0.0	0.0	0.0	0.0	584.1
CT2	0.0	0.0	509.1	0.0	0.0	0.0	0.0	-796.7

	a610	a611	a612	a613	a614	a615	b616	CT1	CT2
a601	-0.1	-42.4	6.9	2.7	-9.0	0.0	0.0	0.0	0.0
a602	-15.8	-10.7	23.7	-2.7	0.9	-2.6	0.0	0.0	0.0
a603	19.4	-1.2	-2.8	4.1	-8.5	8.3	-4.0	-806.6	509.1
a604	-3.7	-4.5	3.2	2.0	-6.2	1.4	2.7	0.0	0.0
b606	-2.1	0.0	2.5	2.1	0.0	-2.0	-1.3	0.0	0.0
b607	1.8	0.0	3.3	3.9	-2.9	-4.8	-0.2	0.0	0.0
b608	75.6	7.4	-0.7	0.0	0.0	3.8	19.4	0.0	0.0
a609	-8.4	6.5	-1.5	-5.6	0.0	-10.8	12.5	584.1	-796.7
a610	15440.5	-42.4	38.8	9.7	-0.3	5.0	8.9	0.0	0.0
a611	-42.4	15515.7	223.2	-10.1	-0.7	0.0	0.0	0.0	0.0
a612	38.8	223.2	15639.3	1.6	3.2	0.0	0.0	0.0	0.0
a613	9.7	-10.1	1.6	15625.4	-63.5	0.0	0.0	0.0	0.0
a614	-0.3	-0.7	3.2	-63.5	15647.1	0.0	0.0	0.0	0.0
a615	5.0	0.0	0.0	0.0	0.0	15606.2	2.7	0.0	0.0
b616	8.9	0.0	0.0	0.0	0.0	2.7	16124.9	0.0	0.0
CT1	0.0	0.0	0.0	0.0	0.0	0.0	0.0	18220.7	-12.6
CT2	0.0	0.0	0.0	0.0	0.0	0.0	0.0	-12.6	20750.9

To compute the absorption spectra, we employ the vibronic model developed for the ML-MCTDH simulations (Fig. S8). From the diabatic energy gradients shown in Fig. S8a, we derive the reorganization energies and map each normal mode onto an underdamped Brownian oscillator with frequency ω_k, reorganization λ_k, and damping factor $\gamma = 5\,\mathrm{cm}^{-1}$:[13]

$$J_{\mathrm{vib}}(\omega) = \sum_k 2\lambda_k \frac{\omega_k^2 \gamma\, \omega}{\left(\omega^2 - \omega_k^2\right)^2 + \gamma^2\omega^2}. \tag{S6}$$

The frequencies and reorganization energies are taken from the full LVC model containing 427 modes. This mapping is repeated for the four diabatic electronic states. For the spectra calculations, we use the average of the a603 and a609 spectral densities (λ_{vib}=709 cm^{-1}) for all LE states, whereas for the CT states we adopt their specific ones.

The low-frequency protein and environmental motions are modeled using overdamped Brownian spectral densities, which is equivalent to the first positive-frequency term of the shifted Drude–Lorentz oscillators (Eq. S5). The parameters are taken from Ref. 5, namely $\lambda^{\mathrm{env}}_{\mathrm{LE}} = 60$ cm^{-1}, $\lambda^{\mathrm{env}}_{\mathrm{a603^+a609^-}} = 1337$ cm^{-1}, $\lambda^{\mathrm{env}}_{\mathrm{a603^-a609^+}} = 941$ cm^{-1}, and $\gamma_{\mathrm{env}} = 30$ cm^{-1}. The total vibrational-environmental spectral densities are reported in Fig. S6.

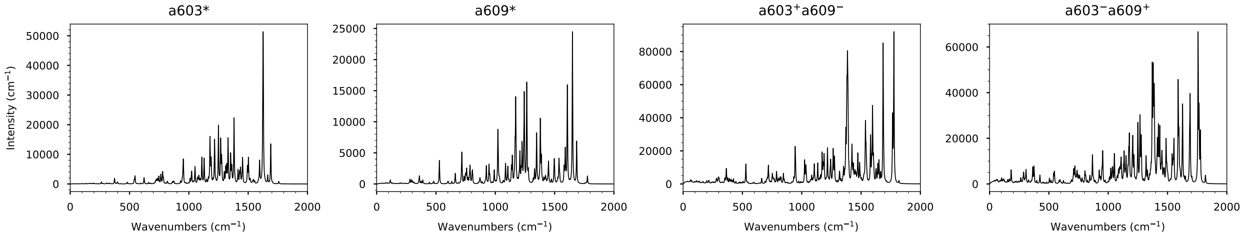

Figure S6: *Total (environmental + vibrational) spectral densities of the different states of the a603-a609 dimer used for the calculation of absorption spectra, each in a different panel. The total vibrational reorganization energies are reported in Fig. S8a.*

The absorption spectra are then computed using the *Full Cumulant Expansion* (FCE) lineshape theory.[14] In this framework, the linear absorption is given by

$$A(\omega) \propto \sum_{ij} A_{ij}(\omega) \text{ with } A_{ij} = \omega\ \mathrm{Re} \int_{-\infty}^{+\infty} \mathrm{d}t\; e^{i\omega t} \mathbf{I}_{ij}(t) \mathbf{M}_{ij}, \tag{S7}$$

where $\mathbf{M}_{ij} = \vec{\mu_i} \cdot \vec{\mu_j}$ is the dipole strength matrix. The absorption tensor $\mathbf{I}(t)$ is

$$\mathbf{I}(t) = e^{-iH_{\mathrm{el}}t} e^{-\mathbf{K}(t)}, \tag{S8}$$

and the lineshape matrix in the eigenstate basis is defined as

$$K_{ab}(t) = \sum_c \sum_i c^*_{ia} |c_{ic}|^2 c_{ib} \int_0^t \mathrm{d}t_2 \int_0^{t_2} \mathrm{d}t_1 e^{i\omega_{ac}t_2 - i\omega_{bc}t_1} C_i(t_1), \tag{S9}$$

Here, we indicate with i, j the localized basis, while with a, b the delocalized basis of the Hamiltonians eigenstates. Moreover, $\hbar\omega_{ac} = E_a - E_c$ is the energy difference between states a, c and $C_i(t)$ is the bath-correlation function of state i, i.e., the Fourier transform of its spectral density $J_i(\omega)$. The FCE lineshape inherently includes all off-diagonal (non-secular) terms and captures non-Markovian effects of the bath.

For each MD snapshot the absorption spectrum is computed independently and then averaged to obtain the final spectrum. The spectra are reported in Fig. 4a and commented in the main text.

We take advantage of our spectra calculations also to justify the neglect of the Chls other than a603 and a609 in the quantum dynamics. To do so, we calculate the spectra by setting to zero the couplings between the dimer (i.e. a603*,a609*,a603$^+$a609$^-$,a603$^-$a609$^+$) and the other Chls. The result is shown in dashed red line in Fig. S7 (“Total”), compared with the spectrum calculated by including all Chl-Chl couplings (solid blue line). The two spectra almost overlap, suggesting that, at least in linear spectroscopy, the a603-a609 dimer is separable from the rest of the rest of Lhca4. To further support this conclusion, we quantify the contributions of the a603/a609 dimer to the total absorption spectrum. To do so, we sum over A_{ij} (Eq. S7) over i, j belonging to the four states $\{a603^*, a609^*, a603^+a609^-, a603^-a609^+\}$. The results are shown in Fig. S7 (“Dimer contribution”), again as solid blue line (full model) and dashed red line (uncoupled dimer).

Also in this case the lines almost overlap, further confirming that the dimer is separable from the rest of the complex.

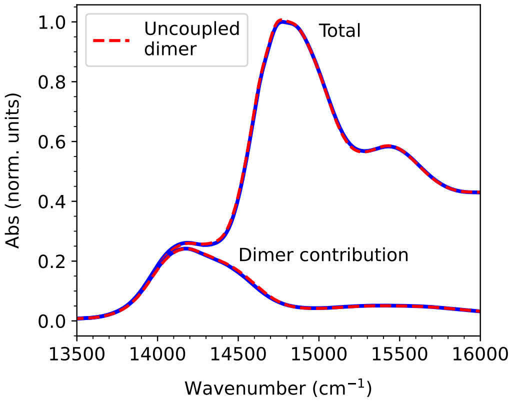

Figure S7: *Total absorption spectra and a603-a609 dimer contribution (77 K). Blue solid lines indicate the spectra calculated using the full Hamiltonians, while to calculate the spectra in red dashed lines we have set to zero the couplings between the dimer (i.e.* $a603^*$*,*$a609^*$*,*$a603^+a609^-$*,*$a603^-a609^+$*) and the other Chls. All spectra are calculated using the Hamiltonians from simulations MD1, MD2, MD3, MD4.*

S6 Supplementary figures

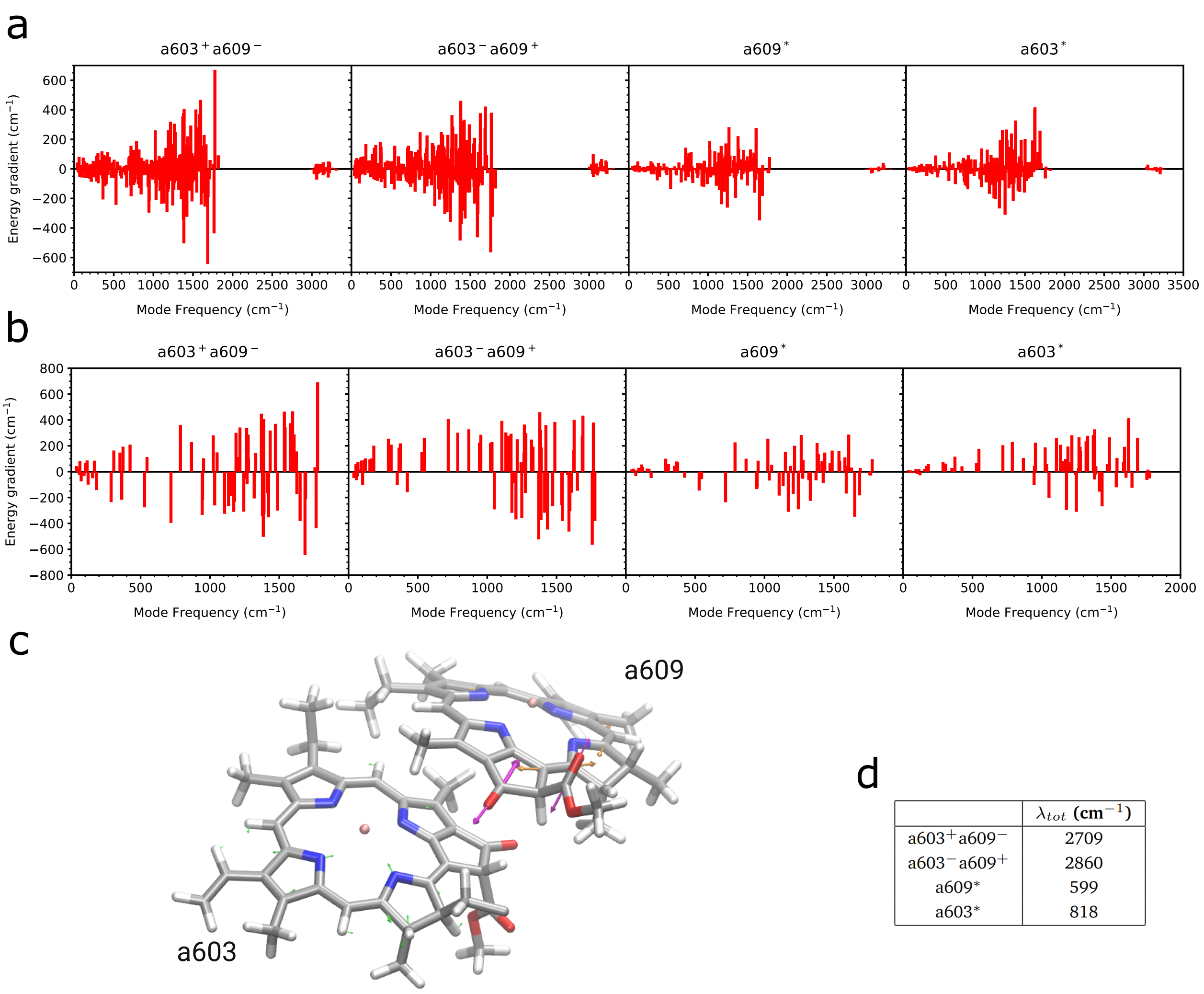

	λ_{tot} (cm^{-1})
a603$^+$a609$^-$	2709
a603$^-$a609$^+$	2860
a609*	599
a603*	818

mode 293, 1385 cm^{-1} (mode 51 in the 72-modes model): C-C and C-N stretchings localized on a603
mode 369, 1686 cm^{-1} (mode 68 in the 72-modes model): C=C stretchings localized on a609
mode 375, 1777cm^{-1} (mode 72 in the 72-modes model): C=O stretchings localized on a609

Figure S8: *(a) LVC parameters of diabatic energies and corresponding vibrational frequencies calculated for the LE and CT states of the a603-a609 dimer from the optimized*[5] *Lhca4 crystal structure.*[15] *This model contains 437 normal modes, corresponding to the modes of the whole dimer. (b) LVC parameters for the reduced 72 modes model. (c) Representation of a603-a609 dimer; arrows indicate the vibrations with higher coupling to the diabatic energies. Different normal modes are indicated with arrow of different colors. (d) Total reorganization energy of each diabatic state.*

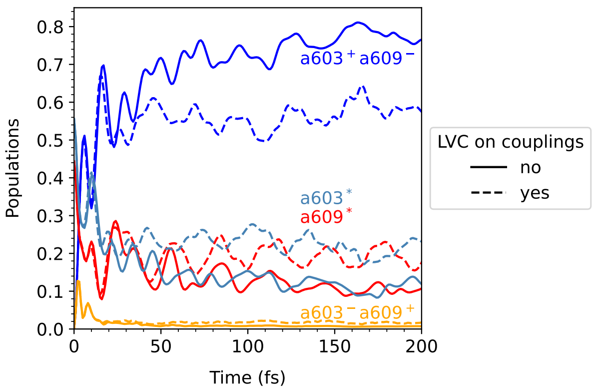

Figure S9: *Population dynamics for a single frame (case 1, $E_{CT} > E_{LE}$) extracted from MD simulations (MD2). The solid lines represent the dynamics obtained by neglecting the LVC parameters on coupling (g_{ij}^k=0, $i \neq j$), while the dashed lines show the populations obtained by including these parameters.*

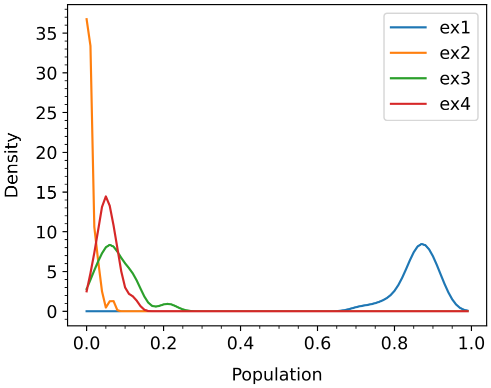

Figure S10: ***Distribution over MD2 of the delocalized diabatic states, obtained by initially populating the bright exciton and transforming it into the localized diabatic basis. This state is then used as the initial state for the ML-MCTDH dynamics****. The distributions are obtained using Gaussian kernels for a kernel-density estimate.*

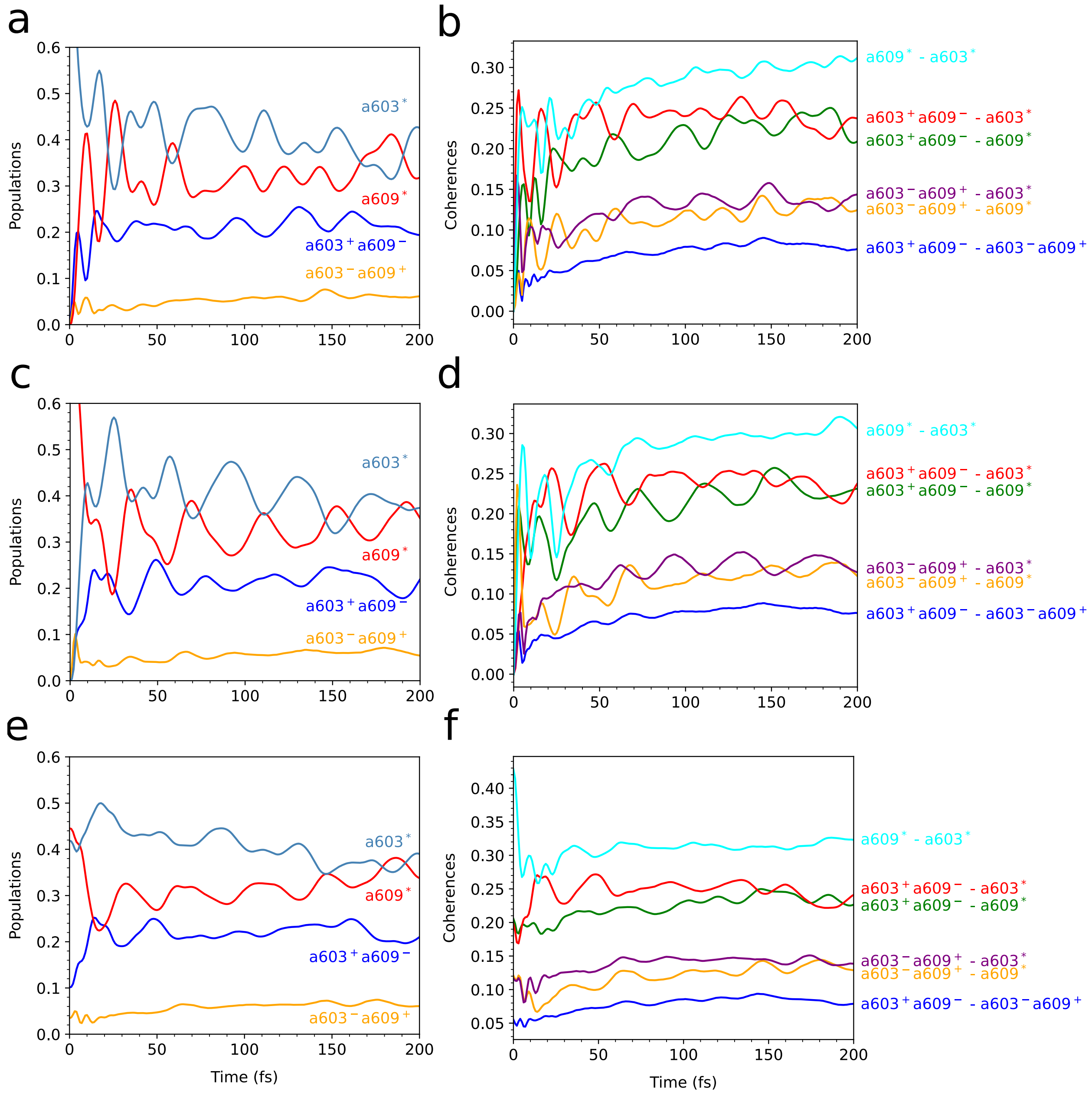

Figure S11: *(a,c,e) Populations and (b,d,f) coherences* ***(absolute value)*** *dynamics calculated using the ML-MCTDH method for the a603-a609 dimer, with the initial state set on a603* (a,b), a609* (c,d) and the delocalized diabatic state ex*$_1$ *(e,f). The results are averaged over the molecular dynamics simulation (MD2 of Ref. 5).*

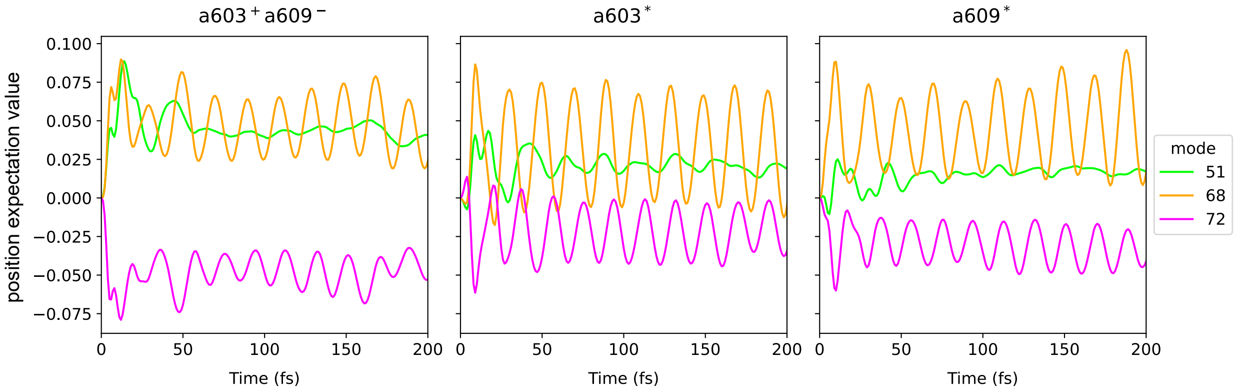

Figure S12: *Expectation values of the position operator for the three modes with highest reorganization energies, projected onto the a603$^+$a609$^-$ CT state (left panel), the a603* state (central panel) and the a609* state (right panel). The expectation values are averaged over the frames extracted from the MD simulation (MD2 of Ref. 5). The numbers of the normal modes indicated in the legend refer to the 72-modes model.*

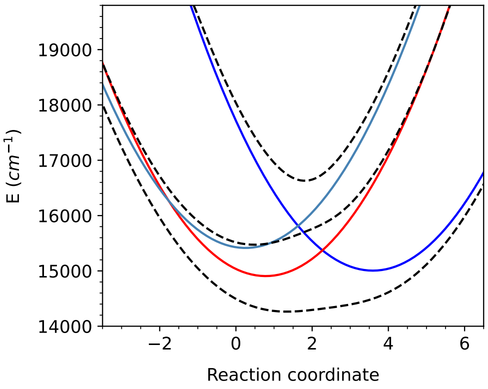

Figure S13: *Potential energy surfaces of the diabatic states (solid lines), along the direction connecting the minimum of the ground state to the minimum of the CT state, for one MD frame (intermediate between case 1 and case 2) where the energy of the CT state is similar to that of the LE states. The adiabatic eigenstates (S_1, S_2, S_3) are shown in black dashed lines. The color scheme is identical to Figure 3 in the main text.*

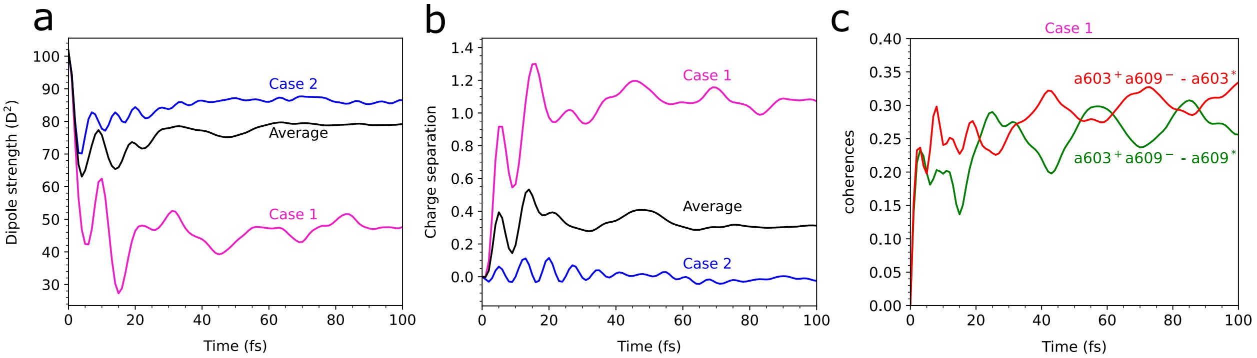

Figure S14: *(a) Dipole strength (defined in Eq. 8) and (b) charge separation (defined in Eq. 9) along the ML-MCTDH dynamics. The black lines show the results averaged over the Molecular Dynamics simulation (MD2 of Ref. 5). Instead, the magenta and blue lines show the MD snapshots introduced in Fig. 3, named case 1 and case 2 respectively. (c) Coherences* ***(absolute value)*** *between the LE states and the $a603^*a609^-$ state, for the case 1.*

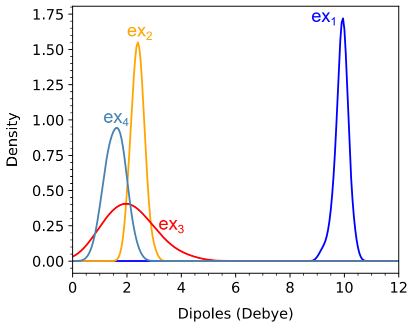

Figure S15: *Distributions of the transition dipoles for the delocalized diabatic states. The dipoles used are from the Molecular Dynamics simulation (MD2 of Ref. 5). The distributions are obtained using Gaussian kernels for a kernel-density estimate.*

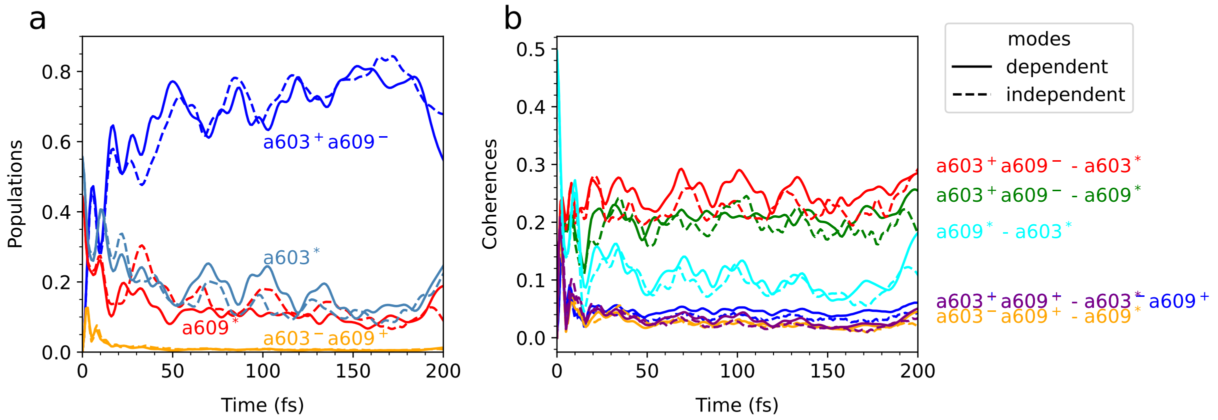

Figure S16: *Dynamics of populations (a) and coherences* **(absolute value)** *(b) for a single frame (case 1, $E_{CT} > E_{LE}$) from MD2 simulations. Modes with reorganization energy below 50 cm^{-1} in all diabatic states are excluded, yielding a 20-mode model (solid lines), where modes are shared across electronic states. Dashed lines show a model with 80 independent modes, each state coupled to its own copy.*

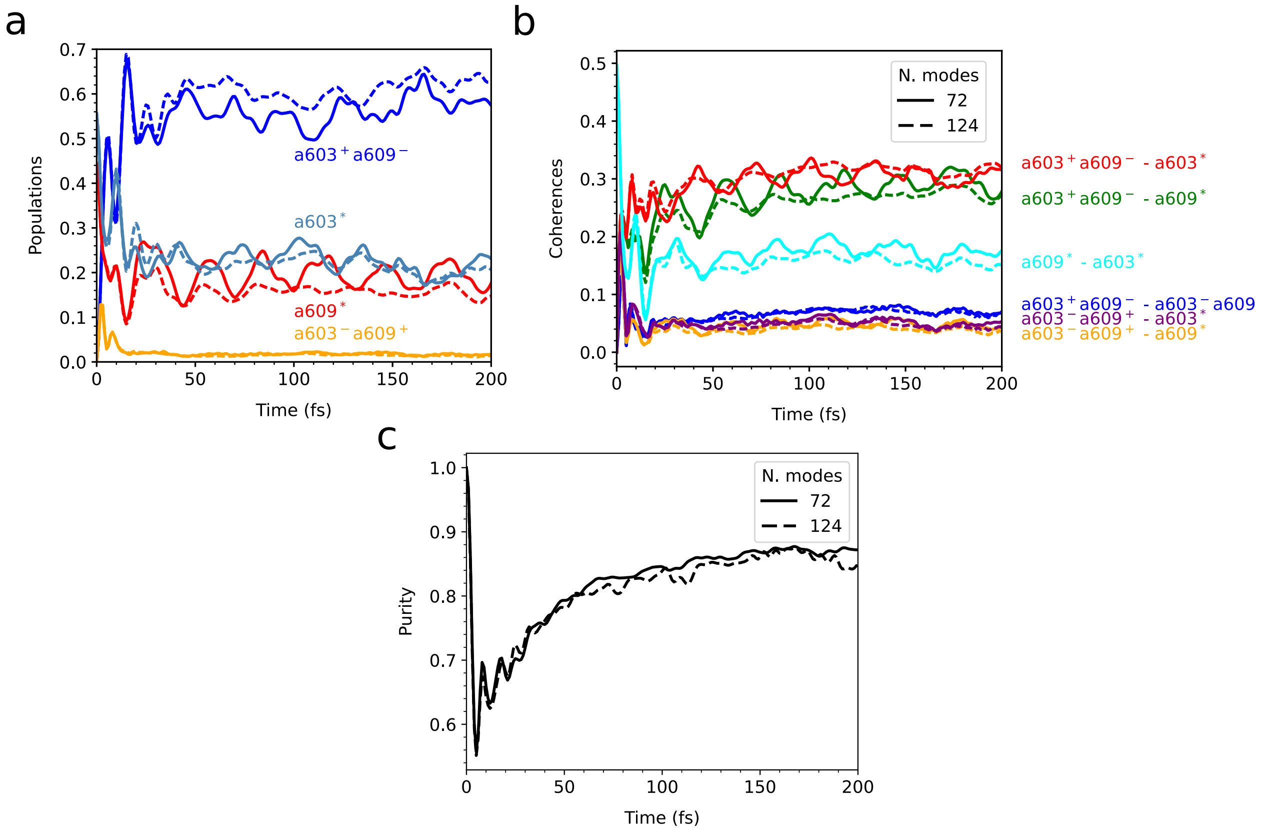

Figure S17: *Dynamics of populations (a), coherences* **(absolute value)** *(b) and density matrix purity (c) for a single frame (case 1, $E_{CT} > E_{LE}$) from MD2 simulations. Modes with reorganization energy below a cutoff in all diabatic states are excluded. Solid lines: 72-mode model (cutoff = 20 cm^{-1}). Dashed lines: 124-mode model (cutoff = 10 cm^{-1}).*

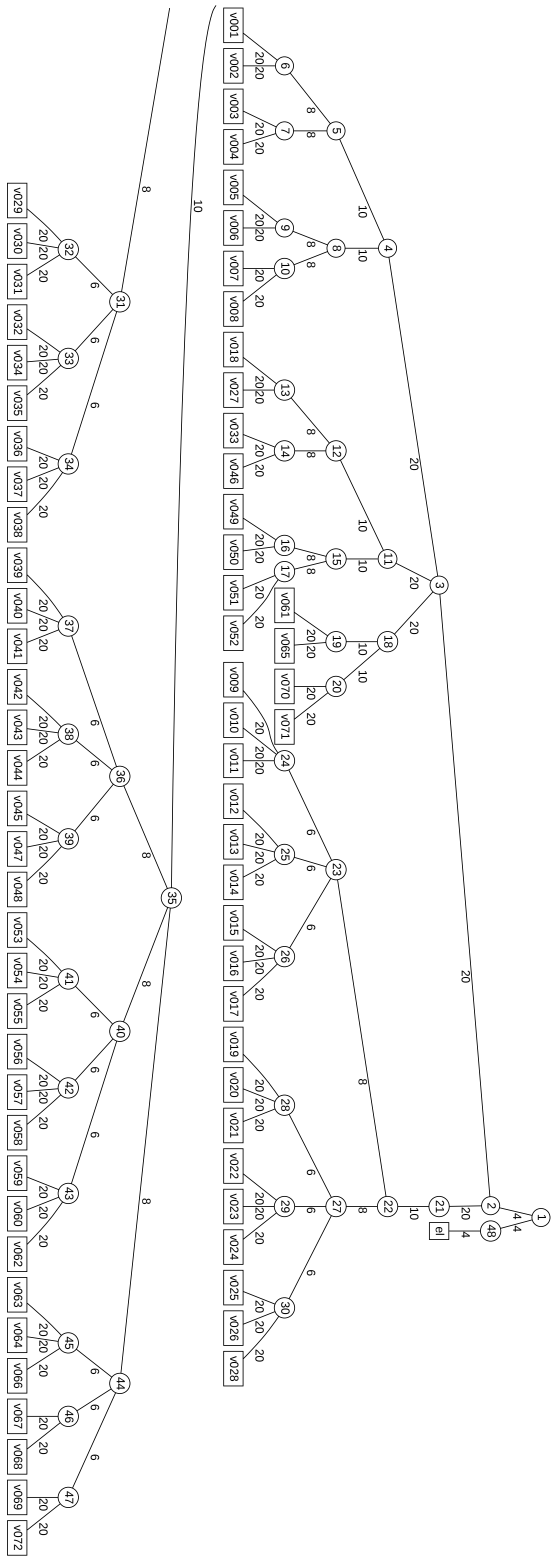

Figure S18: *ML-MCTDH tree used for the simulations of the a603-a609, using the 72 modes reduced model. The numbers of single particle functions used to describe each layer have been indicated on the lines connecting the corresponding layers of the tree.*

References

(1) Vendrell, O.; Meyer, H.-D. Multilayer multiconfiguration time-dependent Hartree method: Implementation and applications to a Henon–Heiles Hamiltonian and to pyrazine. *J. Chem. Phys.* **2011**, *134*, 044135.

(2) Wang, H.; Thoss, M. Multilayer formulation of the multiconfiguration time-dependent Hartree theory. *J. Chem. Phys.* **2003**, *119*, 1289–1299.

(3) Beck, M. H.; Jäckle, A.; Worth, G. A.; Meyer, H.-D. The multiconfiguration time-dependent Hartree (MCTDH) method: a highly efficient algorithm for propagating wavepackets. *Phys. Rep.* **2000**, *324*, 1–105.

(4) Manthe, U. A multilayer multiconfigurational time-dependent Hartree approach for quantum dynamics on general potential energy surfaces. *J. Chem. Phys.* **2008**, *128*, 164116.

(5) Sláma, V.; Cupellini, L.; Mascoli, V.; Liguori, N.; Croce, R.; Mennucci, B. Origin of Low-Lying Red States in the Lhca4 Light-Harvesting Complex of Photosystem I. *J. Phys. Chem. Lett.* **2023**, *14*, 8345–8352.

(6) Wales, D. J.; Doye, J. P. K. Global Optimization by Basin-Hopping and the Lowest Energy Structures of Lennard-Jones Clusters Containing up to 110 Atoms. *J. Phys. Chem. A* **1997**, *101*, 5111–5116.

(7) Virtanen, P.; Gommers, R.; Oliphant, T. E.; Haberland, M.; Reddy, T.; Cournapeau, D.; Burovski, E.; Peterson, P.; Weckesser, W.; Bright, J.; van der Walt, S. J.; Brett, M.; Wilson, J.; Millman, K. J.; Mayorov, N.; Nelson, A. R. J.; Jones, E.; Kern, R.; Larson, E.; Carey, C. J.; Polat, I.; Feng, Y.; Moore, E. W.; VanderPlas, J.; Laxalde, D.; Perktold, J.; Cimrman, R.; Henriksen, I.; Quintero, E. A.; Harris, C. R.; Archibald, A. M.; Ribeiro, A. H.; Pedregosa, F.; van Mulbregt, P.; Vijaykumar, A.; Bardelli, A. P.; Rothberg, A.; Hilboll, A.; Kloeckner, A.; Scopatz, A.; Lee, A.;

Rokem, A.; Woods, C. N.; Fulton, C.; Masson, C.; Häggström, C.; Fitzgerald, C.; Nicholson, D. A.; Hagen, D. R.; Pasechnik, D. V.; Olivetti, E.; Martin, E.; Wieser, E.; Silva, F.; Lenders, F.; Wilhelm, F.; Young, G.; Price, G. A.; Ingold, G.-L.; Allen, G. E.; Lee, G. R.; Audren, H.; Probst, I.; Dietrich, J. P.; Silterra, J.; Webber, J. T.; Slavič, J.; Nothman, J.; Buchner, J.; Kulick, J.; Schönberger, J. L.; de Miranda Cardoso, J. V.; Reimer, J.; Harrington, J.; Rodríguez, J. L. C.; Nunez-Iglesias, J.; Kuczynski, J.; Tritz, K.; Thoma, M.; Newville, M.; Kümmerer, M.; Bolingbroke, M.; Tartre, M.; Pak, M.; Smith, N. J.; Nowaczyk, N.; Shebanov, N.; Pavlyk, O.; Brodtkorb, P. A.; Lee, P.; McGibbon, R. T.; Feldbauer, R.; Lewis, S.; Tygier, S.; Sievert, S.; Vigna, S.; Peterson, S.; More, S.; Pudlik, T.; Oshima, T.; Pingel, T. J.; Robitaille, T. P.; Spura, T.; Jones, T. R.; Cera, T.; Leslie, T.; Zito, T.; Krauss, T.; Upadhyay, U.; Halchenko, Y. O.; Vázquez-Baeza, Y. SciPy 1.0: fundamental algorithms for scientific computing in Python. *Nat. Methods* **2020**, *17*, 261–272.

(8) Tanimura, Y. Numerically "exact" approach to open quantum dynamics: The hierarchical equations of motion (HEOM). *J. Chem. Phys.* **2020**, *153*, 020901.

(9) Liu, H.; Zhu, L.; Bai, S.; Shi, Q. Reduced quantum dynamics with arbitrary bath spectral densities: Hierarchical equations of motion based on several different bath decomposition schemes. *J. Chem. Phys.* **2014**, *140*, 134106.

(10) Olbrich, C.; Kleinekathöfer, U. Time-Dependent Atomistic View on the Electronic Relaxation in Light-Harvesting System II. *J. Phys. Chem. B* **2010**, *114*, 12427–12437.

(11) Kramer, T.; Noack, M.; Reinefeld, A.; Rodríguez, M.; Zelinskyy, Y. Efficient calculation of open quantum system dynamics and time-resolved spectroscopy with distributed memory HEOM (DM-HEOM). *J. Comput. Chem.* **2018**, *39*, 1779–1794.

(12) Wientjes, E.; Roest, G.; Croce, R. From red to blue to far-red in Lhca4: How does

the protein modulate the spectral properties of the pigments? *Biochim. Biophys. Acta (BBA) - Bioenerg.* **2012**, *1817*, 711–717.

(13) Bennett, D. I. G.; Malý, P.; Kreisbeck, C.; van Grondelle, R.; Aspuru-Guzik, A. Mechanistic Regimes of Vibronic Transport in a Heterodimer and the Design Principle of Incoherent Vibronic Transport in Phycobiliproteins. *J. Phys. Chem. Lett.* **2018**, *9*, 2665–2670.

(14) Ma, J.; Cao, J. Förster resonance energy transfer, absorption and emission spectra in multichromophoric systems. I. Full cumulant expansions and system-bath entanglement. *J. Chem. Phys.* **2015**, *142*, 094106.

(15) Mazor, Y.; Borovikova, A.; Caspy, I.; Nelson, N. Structure of the plant Photosystem I supercomplex at 2.6 Å resolution. *Nat. Plants* **2017**, *3*, 17014.